Springer

Acta Mechanica Sinica

CrossMark click for updates

• RESEARCH PAPER •

Acta Mech. Sin., Vol. 39, 122322 (2023)
https://doi.org/10.1007/s10409-022-22322-x

Nonlinear static and dynamic mechanical behaviors of Nb_3Sn superconducting composite wire: experiment and analysis

Lang Jiang[1,2], Xingyi Zhang[1,2*], and You-He Zhou[1,2]

[1] *Key Laboratory of Mechanics on Disaster and Environment in Western China attached to the Ministry of Education of China, Lanzhou University, Lanzhou 730000, China;*

[2] *Department of Mechanics and Engineering Sciences, College of Civil Engineering and Mechanics, Lanzhou University, Lanzhou 730000, China*

Received August 23, 2022; accepted October 31, 2022; published online December 12, 2022

In this paper, the nonlinear mechanical behaviors of Nb_3Sn superconducting composite wires have been investigated by the quasi-static loading-unloading tensile and fatigue tests at the temperature of 77 and 300 K, respectively, which indicates that the quasi-static stress-strain curves and energy dissipations exhibit strong nonlinearity. Meanwhile, the nonlinear and linear unloading modulus are derived by considering the damage degradation, and the elastic-plastic constitutive is proposed to predict the quasi-static loading-unloading stress-strain responses and energy dissipation. Moreover, the damage evolution model has been conducted to elucidate the energy dissipation of fatigue tests for the Nb_3Sn composite wire at the temperature of 77 and 300 K. The combination of experimental and theoretical results indicates that the nonlinearity of energy dissipation is caused by damage degradation during quasi-static loading and unloading tensile tests. Furthermore, the fatigue fracture modes of Nb_3Sn composite wires also have been analyzed, which indicated that the Nb_3Sn sub-elements show brittle fracture at the temperature of 77 K while ductile fracture at the temperature of 300 K. These findings provide novel insights into the nonlinear mechanical behaviors of Nb_3Sn superconducting composite wires.

Nonlinearity, Elastic-plastic constitutive, Energy dissipation, Damage degradation, Nb_3Sn composite wires

Citation: L. Jiang, X. Zhang, and Y.-H. Zhou, Nonlinear static and dynamic mechanical behaviors of Nb_3Sn superconducting composite wire: experiment and analysis, Acta Mech. Sin. **39**, 122322 (2023), https://doi.org/10.1007/s10409-022-22322-x

1. Introduction

The international thermonuclear experimental reactor (ITER) is the largest and most complex experimental fusion facility with the stored energy of 51 GJ [1-4]. Due to high critical current density and reasonable price, Nb_3Sn superconducting composite wires have been selected for the central solenoid and toroidal field coils to carry capacity in the ITER [5,6]. Moreover, Nb_3Sn composite wires may become a candidate superconducting material for cutting-edge high-field magnets such as the future circular collider [7]. In the application to Nb_3Sn composite wires, which undergo extremely complex working conditions such as low temperature, strong magnetic field and large current, and also withstand cyclic electromagnetic and thermal loading. These harsh working conditions will undoubtedly lead to the degradation of Nb_3Sn composite wires' performance, which is a key engineering and science topic [8,9]. Over the past decades, numerous experiments and theoretical analyses have been carried out to focus on the effects of mechanical deformation for Nb_3Sn composite wires on the critical current density [7,10-16], critical magnetic field [17,18] and current sharing temperature [19-21]. In general, Nb_3Sn composite wires are composed of brittle superconducting multifilament embedded in a ductile matrix exhibiting strongly nonlinear deformation [22]. Therefore, the nonlinear mechanical behaviors of Nb_3Sn composite wire are mainly challenging obstacles to the development for high-field superconducting magnets [23].

*Corresponding author. E-mail address: zhangxingyi@lzu.edu.cn (Xingyi Zhang)
Executive Editor: Zhong Zhang

Nonlinear mechanical behavior in the loading-unloading process is one of the long-standing issues for metal matrix composites. The isotropic hardening model is the simplest elastic-plastic model to describe the stress-strain response in the loading-unloading process, in which the yield surface is only an extension without translation, but it cannot describe asymmetric plastic behavior. To overcome this problem of the isotropic hardening model, Prager [24] and Ziegler [25] proposed the linear kinematic hardening model, where the translation of the yield surface has been described by the evolution of the back stress. Subsequently, Armstrong et al. [26] introduced a nonlinear kinematic hardening model, which is better to describe nonlinear mechanical behaviors. Chaboche [27] improved the kinematic hardening model with multiple kinematic hardening terms and combined with the isotropic hardening model. With the increasing complexity in nonlinear loading-unloading deformation, multiple-yield surface models have been proposed [28-31]. Among them, the two-yield surface models are widely used because of relatively few parameters, the transient Bauschinger effect, work-hardening stagnation and permanent softening in large elastic-plastic deformation [28,29,32,33]. Numerous previous works have expanded the two-yield surface model [34-37]. For example, Sun and Wagoner [38] proposed a two-yield surface model, named as the quasi-plastic-elastic (QPE) model, to describe the nonlinear loading and unloading behaviors of dual-phase steel. This model introduced the QPE strain due to dislocation pile-up and multiplication, and applied the nonlinear unloading modulus function to describe the complex nonlinear mechanical behaviors. Furthermore, Lee et al. [39] combined the QPE model with a homogeneous anisotropic hardening model to simultaneously capture the unloading and plastic flow behavior. Lee et al. [40] proposed a new QPE model with one yield surface to reduce complexity and computation time without using the two-surface modeling. Hou et al. [41] modified the unloading modulus with power exponential form in the QPE model to describe nonlinear unloading behaviors under compressive deformation. However, the above-mentioned theoretical models do not consider the effects of damage degradation on nonlinear mechanical behaviors.

For the nonlinear mechanical behaviors of Nb_3Sn composite wire, despite that numerous quasi-static loading-unloading experiments have been conducted, the existing elastic-plastic theoretical models do not completely resolve the nonlinear problems [42-46]. For example, in 2005, van den Eijinden et al. [42] constructed the four fitting functions to describe the nonlinear responses of the axial tensile stress-strain curves of Nb_3Sn composite wire manufactured by the bronze routes, internal tin, and powder-in-tube method, respectively, but they are not suitable for all Nb_3Sn composite wires in the full range of strain. In 2011, Bajas [47] developed a nonlinear finite element simulation (FEM) method for modeling the mechanical behavior of Nb_3Sn superconducting composite wires, in which fifth order polynomial function or exponential function were used to fit the behaviors of the envelope curve and the behavior of loading and unloading response. In 2021, Du et al. [48] established a discrete element model of Nb_3Sn superconducting composite wires based on the discretization of the continuum and improved the cohesive model, in which the constitutive models of cohesive model used nonlinear fitting function of Bajas [47]. However, the nonlinear fitting function cannot be used for elastic-plastic constitutive of Nb_3Sn composite wires, and the elastic-plastic constitutive for nonlinear loading-unloading responses is also urgent.

Several elastic-plastic models have been proposed to reveal nonlinear unloading-reloading stress-strain responses. In 2016, Wang et al. [49] developed a multi-filament twist FEM model considering the influence of breakage of filaments to explore elastic-plastic behaviors of Nb_3Sn composite wires, where copper and bronze matrix were treated as combined hardening materials, and Nb_3Sn filaments were treated as elastic materials. In 2019, Lenoir et al. [46] established the multiscale model of Nb_3Sn composite wires, in which copper was modeled with elastic-plastic behavior considering kinematic and isotropic hardenings, and homogenized the superconducting filamentary area using the representative volume element. Therefore, combining experimental and numerical results, it can be found that the existing elastic-plastic models do not precisely describe nonlinear stage during the unloading process and have redundant fitted parameters.

To the best of our knowledge, studies on the fatigue behaviors of Nb_3Sn composite wires are still lacking. In 1979, Cogan et al. [50] presented the simulated model of two-component composites with perfect elastic Nb_3Sn filaments in a ductile matrix to analyze the fatigue behaviors of Nb_3Sn composite wires at cyclic load, which can well predicate the residual stress and matrix yield strength. In 2021, Riccioli [51] conducted the fatigue tests on the Nb_3Sn composite wires under cyclic tensile and compressive stresses at both cryogenic and room temperature, and obtained the strain evolution with fatigue cycles. Jiang et al. [52] investigated the damage evolution of Nb_3Sn composite wires under asymmetric strain cycling of various strain peaks and ranges at room temperature, and analyzed the nonlinear change of stiffness degradation and plastic accumulation with fatigue cycles. Nevertheless, these previous investigations have limited capability to explore fatigue mechanical behaviors of Nb_3Sn composite wires.

It is worth noting that, for the nonlinear mechanical behaviors of Nb_3Sn composite wires, there are still three key problems that need to be explored: (1) Can the QPE model solve the nonlinear mechanical behaviors during the quasi-

static loading-unloading process? (2) If the QPE model does not resolve this problem, how can we establish a new elastic-plastic model? (3) Whether the energy dissipation characteristics of Nb_3Sn composite wires during the fatigue process are the same at the temperature of 77 and 300 K? In this work, the quasi-static loading-unloading and fatigue tests of Nb_3Sn composite wires are conducted at the temperature of 77 and 300 K to analyze its nonlinear mechanical behaviors. Meanwhile, new linear and nonlinear unloading moduli are derived by considering damage degradation, and the quasi-static elastic-plastic constitutive is proposed. In addition, the damage evolution model is derived by considering the proposed three-parameter damage model to obtain the energy dissipation during the fatigue tests of Nb_3Sn composite wires.

The paper is organized as follows. In Sect. 2, the experimental materials and methods of static loading-unloading tests and strain fatigue tests for Nb_3Sn composite wires are discussed. Section 3 is the experimental results. In Sect. 4, the unloading modulus is derived, and the quasi-static elastic-plastic constitutive is established. Section 5 introduced the damage evolution model and obtained the energy dissipation during fatigue processes. The discussions and concluding remarks are presented in Sects. 6 and 7, respectively.

2. Experiments and methods

2.1 Materials

Nb_3Sn superconducting composite wires are multi-filaments twist composites, where its matrix is bronze or copper, and Nb_3Sn sub-elements contained Nb filaments, Cu and Ta [53]. In this work, the Nb_3Sn superconducting composite wires were manufactured by the inner tin method [54] from Western Superconducting Technologies Co. Ltd. Nb_3Sn superconducting composite wires consisted of 50% Cu matrix and 50% Nb_3Sn sub-elements. Nb_3Sn superconducting composite wires were heat-treated: 210 °C × 50 h + 340 °C × 25 h + 450 °C × 25 h + 575 °C × 100 h + 650 °C × 100 h. The diameter of all samples was 0.81 mm, and the length of the interception was 152 mm, as shown in Fig. 1.

2.2 Test methods

The quasi-static loading-unloading tests of Nb_3Sn superconducting composite wires were conducted with the electronic universal testing machine at 77 and 300 K. The loading rates were all set at 0.1 mm/min during the loading and unloading processes, respectively. Two samples were performed for each test. For the fatigue cyclic testing, the strain-controlled tension-tension fatigue tests were conducted with INSTRON 8802 fatigue machine at 77 and 300 K (see Fig. 2), and the sine cyclic waveform was applied at a frequency of 2 Hz during fatigue tests. The fatigue strain range ($\Delta\varepsilon$) for Nb_3Sn composite wires varies from 0.005 to 0.0065, and the strain peak is 0.03. For each group of tests, at least two samples were performed.

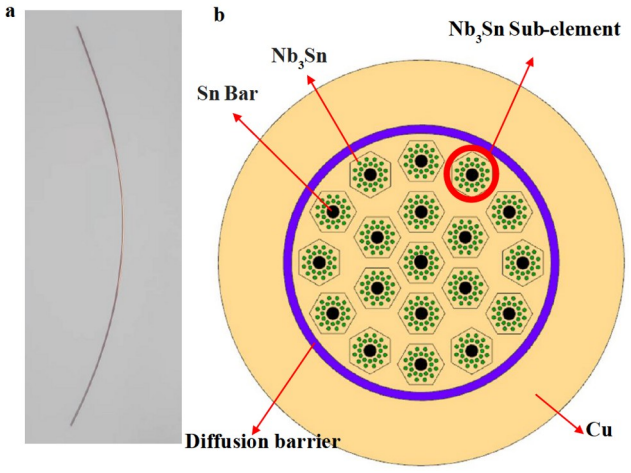

Figure 1 **a** Nb_3Sn superconducting composite wires; **b** the schematic of cross section for Nb_3Sn superconducting composite wires.

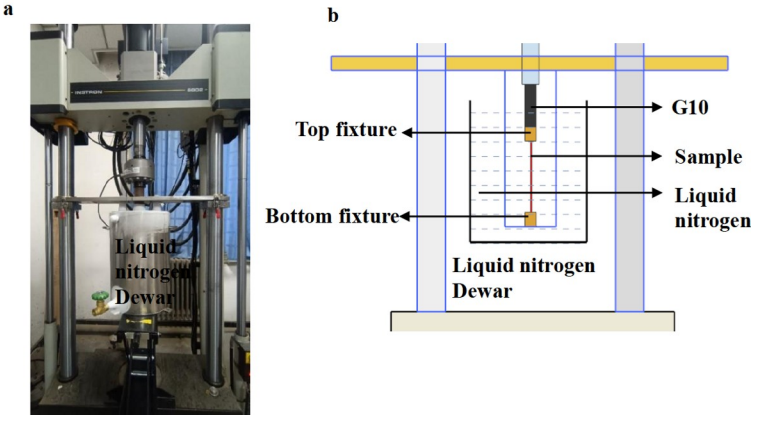

Figure 2 **a** Electronic universal testing machine; **b** the schematic of INSTRON fatigue machine, where G10 is adiabatic epoxy.

3. Experimental results

3.1 Quasi-static mechanical behaviors

Figure 3 shows the stress-strain curves of Nb_3Sn superconducting composite wires with the temperature of 77 and 300 K. It can be seen that, the Nb_3Sn superconducting composite wires exhibit significant nonlinearity during the loading-unloading-reloading processes. Moreover, the nonlinearity at 300 K is more obvious than at 77 K due to the brittle of Nb_3Sn superconducting composite wire of the former being weaker than that of the latter. The nonlinear mechanical response during the unloading-reloading process is caused by the anelastic strain linked with the reversible movements of microstructures, such as the dislocation pile-up and multiplication [55], and the anelastic strain will vanish during the unloading process.

Due to the nonlinear mechanical response, stress-strain hysteresis loops and energy dissipation can occur during loading-unloading processes. By integrating the area of stress-strain hysteresis loops, the relationship between the energy dissipation and unloading stress can be obtained (see Fig. 4), which indicated that the energy dissipations show nonlinearity behaviors with the increase of unloading stress. However, the nonlinearity of energy dissipations for Nb_3Sn superconducting composite wires is different from advanced high-strength steels in Refs [38,39], where the energy dissipations are linearly elevated as the unloading stress increases, which will be detailed interpreted by the elastic-plastic model in Sect. 6.

3.2 Fatigue mechanical behaviors

The stress-strain curves for Nb_3Sn superconducting composite wires during fatigue tests at $\Delta\varepsilon = 0.005$ are shown in Fig. 5, which shows that the nonlinearity of the stress-strain responses at 300 K is larger than the temperature of 77 K during fatigue cycles. With the increase of fatigue cycles

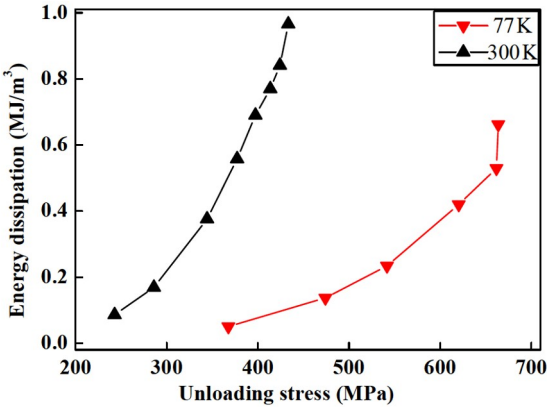

Figure 4 The relationship between energy dissipation and unloading stress for various temperatures.

number, the nonlinearity of the stress-strain responses increases at the temperature of 300 K. Varying nonlinearity of the stress-strain responses will change energy dissipation, so there is an obvious difference in energy dissipation at the temperature of 77 and 300 K.

The relationship between energy dissipation and fatigue cycles number for Nb_3Sn superconducting composite wires with various strain ranges (0.005, 0.0053, and 0.0057) is shown in Fig. 6. It can be seen that energy dissipation increases with increasing fatigue cycles number of cycles at 300 K. However, when the fatigue test temperature is 77 K, the energy dissipations of Nb_3Sn superconducting composite wires show three stages: initially rapid drop, gradually steady and accelerated increase stages, which is the same as what happened to hybrid carbon nanotube/glass fiber/polymer composites [56], caused by residual stresses. In the initial rapid drop stage, the energy dissipation drops sharply due to the thermal residual stress [57] induced by thermal mismatch among the Nb, Sn, Cu and Nb_3Sn in Nb_3Sn superconducting composite wires slowly releases. Subsequently, the Nb_3Sn superconducting composite wires are brittle at 77 K, and energy dissipation changes are slow and

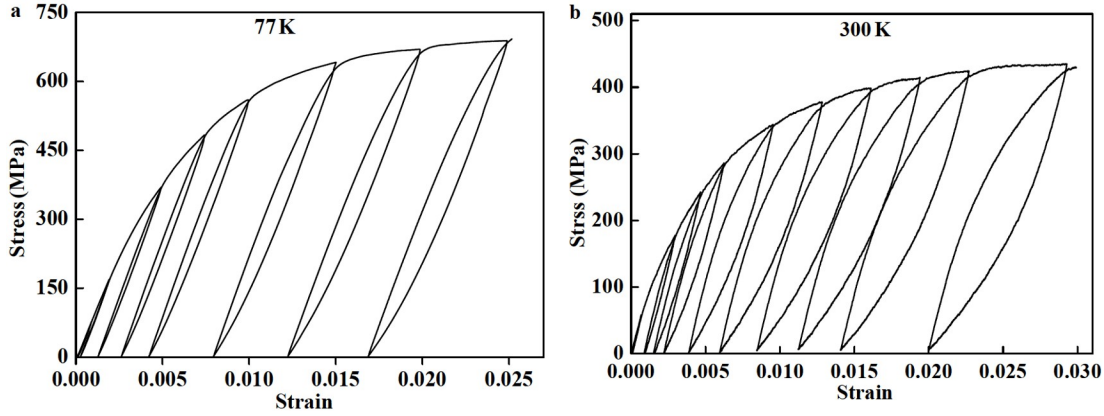

Figure 3 The tensile stress-strain curves during loading-unloading processes of Nb_3Sn composite wires with temperature of **a** 77 K and **b** 300 K.

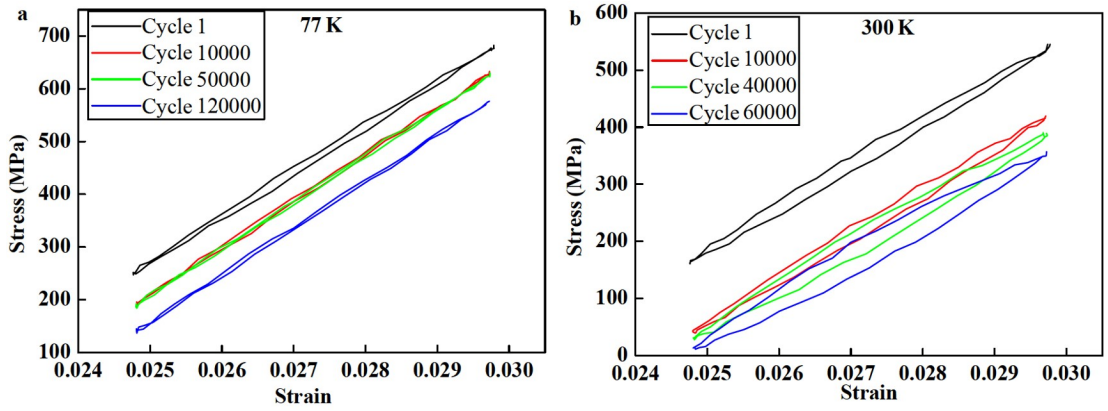

Figure 5 The stress-strain responses for Nb_3Sn superconducting composite wires during fatigue test at $\Delta\varepsilon = 0.005$ with the temperature of **a** 77 K and **b** 300 K.

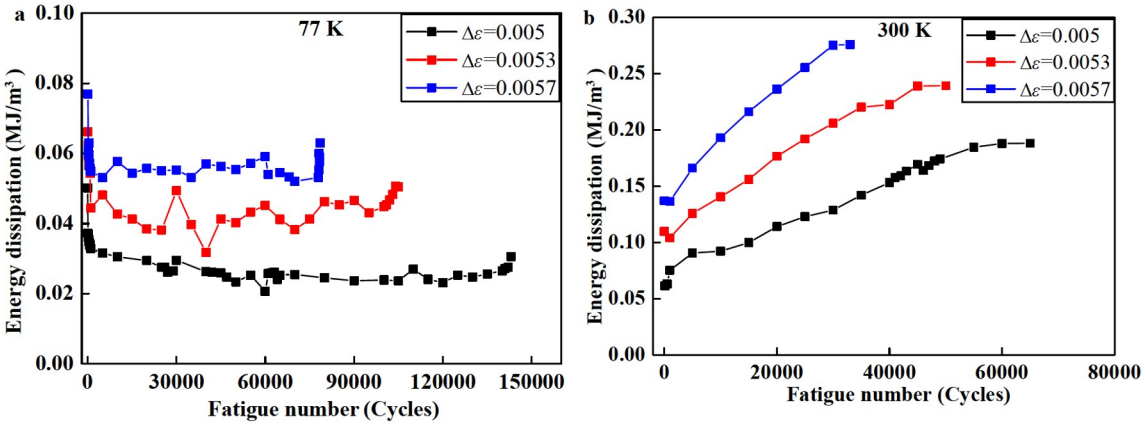

Figure 6 The energy dissipation-fatigue cycles number curves for Nb_3Sn superconducting composite wires for various strain range with the temperature of **a** 77 K and **b** 300 K.

steady in the steady stage. In the accelerated increase stage, a large number of macroscopic cracks were formed, which led to the increase of plastic strain and caused an augment of energy dissipation. More results of fatigue damage have been shown in Sect. 1 of Appendix.

4. Quasi-static elastic-plastic model

4.1 Theory analyses

In Fig. 7, the outer surface called the yield surface represents a transition from elastic or anelastic behavior to plastic elastic. When the stress state is on the yield surface, Nb_3Sn superconducting composite wires will appear plastic deformation and damage. In most of the studies, plastic damage is evaluated by applying the continuum damage mechanics (CDM) [58-60]. However, when the CDM method is applied to nonlinear unloading processes, the number of parameters will increase. To avoid more parameters, a plastic-strain-dependent linear unloading modulus E_{lu} and nonlinear unloading modulus E_{nu} (see Fig. 7) will be derived according to the chord modulus and unloading process.

In classical damage mechanics, the damage could be represented by the degradation of the linear unloading modulus E_{lu}. In general, damage D can be defined as

$$D = 1 - \frac{E_{\mathrm{lu}}}{E_0}, \tag{1}$$

where E_0 is the initial elastic modulus. It can be seen that the degradation of damage can lead to the lower linear unloading modulus E_{lu}.

In Fig. 7a, the anelastic surface can be separated from unloading and reloading processes into linear and nonlinear processes. The linear unloading process refers to going from the point $A(\varepsilon_{\max}, \sigma_{\max})$ to point $B(\varepsilon_0, \sigma_0)$, and the nonlinear unloading process is from the point $B(\varepsilon_0, \sigma_0)$ to point $C(\varepsilon_{\mathrm{p}}, 0)$ (see Fig. 7a). During the unloading process from point A to C, the relationship between strain and stress can be written as

$$E_{\mathrm{chord}}(\varepsilon_{\mathrm{p}} - \varepsilon_{\max}) = \int_{\varepsilon_{\max}}^{\varepsilon_0} E_{\mathrm{lu}} \mathrm{d}\varepsilon + \int_{\varepsilon_0}^{\varepsilon_{\mathrm{p}}} E_{\mathrm{nu}} \mathrm{d}\varepsilon, \tag{2}$$

where E_{chord} is the slope from point A to C, and can be expressed as

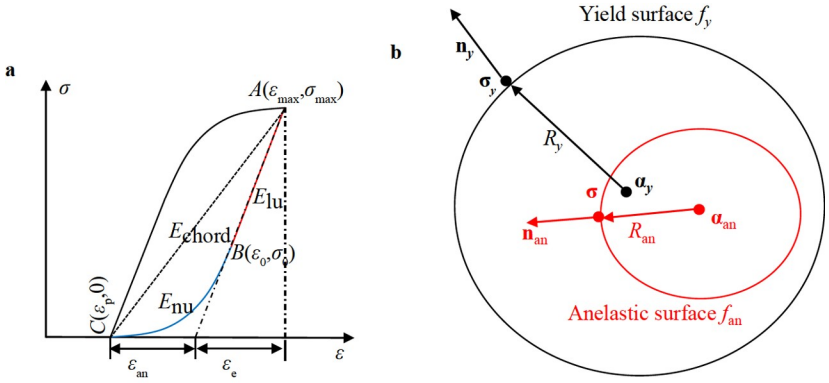

Figure 7 Description of variables in the two-surface model.

$$E_{\text{chord}} = E_0 - K(1-\mathrm{e}^{-\xi p}). \tag{3}$$

Here, $K = E_0 - E_a$, E_a is Young's modulus under infinitely large strain, and ζ is a material constant [61].

In Eq. (2), E_{nu} is a nonlinear unloading modulus between the point $B(\varepsilon_0, \sigma_0)$ to point $C(\varepsilon_{\text{p}}, 0)$. Sun and Wagoner [38] have defined the nonlinear unloading modulus in QPE model, which can be written as

$$E_{\text{nu}} = E_{\text{lu}} - E_1\left(1-\mathrm{e}^{-b_1\left\|\mathrm{d}\varepsilon-\mathrm{d}\varepsilon_{\text{p}}\right\|}\right)(1-\mathrm{e}^{-b_1\left\|\mathrm{d}\varepsilon-\mathrm{d}\varepsilon_{\text{p}}\right\|}), \tag{4}$$

where E_1 and b_1 are material parameters determined from measured loading and unloading stress-strain curves, respectively. E_{nu} is reduced from linear unloading modulus E_{lu} during nonlinear unloading. If no damage degradation, E_{lu} is the initial elastic modulus E_0, which is the same as the QPE model. However, when damage degradation appears, E_{lu} is related to plastic strain, which does not be solved by the QPE model. As follows, E_{lu} considering degradation will be derived according to the relationship between the unloading path and chord modulus.

Substituting Eq. (4) into Eq. (2), that is

$$\begin{aligned} E_{\text{chord}}(\varepsilon_{\text{p}}-\varepsilon_{\max}) = {} & E_{\text{lu}}(\varepsilon_0-\varepsilon_{\max}) + \frac{E_1}{b_1}\mathrm{e}^{-b_1(\varepsilon_0-\varepsilon_{\text{p}})} \\ & - \frac{E_1}{b_1} + (E_{\text{lu}}-E_1)(\varepsilon_{\text{p}}-\varepsilon_0), \end{aligned} \tag{5}$$

and then the linear unloading modulus E_{lu} can be written as

$$E_{\text{lu}} = E_{\text{chord}} + \frac{1}{(\varepsilon_{\max}-\varepsilon_{\text{p}})}\left[\frac{E_1}{b_1}\mathrm{e}^{-b_1(\varepsilon_0-\varepsilon_{\text{p}})} + E_1(\varepsilon_0-\varepsilon_{\text{p}}) - \frac{E_1}{b_1}\right], \tag{6}$$

which reflects the relationship among the chord modulus, plastic strain and linear unloading modulus.

Substituting Eq. (6) into Eq. (4), the nonlinear unloading modulus E_{nu} can be described as

$$\begin{aligned} E_{\text{nu}} = {} & E_{\text{chord}} + \frac{1}{(\varepsilon_{\max}-\varepsilon_{\text{p}})}\left[\frac{E_1}{b_1}\mathrm{e}^{-b_1(\varepsilon_0-\varepsilon_{\text{p}})} + E_1(\varepsilon_0-\varepsilon_{\text{p}}) - \frac{E_1}{b_1}\right] \\ & - E_1\left[1-\mathrm{e}^{-b_1\left\|\mathrm{d}\varepsilon-\mathrm{d}\varepsilon_{\text{p}}\right\|}\right]. \end{aligned} \tag{7}$$

It is worth noting that ε_0 can be considered as

$$\varepsilon_0 = \varepsilon_{\max} - \frac{2R_{\text{an}}(p)}{E_{\text{lu}}}, \tag{8}$$

where $R_{\text{an}}(p)$ represents the size of the linear unloading region [38] between point $A(\varepsilon_{\max}, \sigma_{\max})$ and $B(\varepsilon_0, \sigma_0)$, which can be defined as

$$R_{\text{an}}(p) = A_{\text{an}}\left(1 - B_{\text{an}} \cdot \mathrm{e}^{-\eta_{\text{an}} \cdot p}\right), \tag{9}$$

where A_{an} is the size of the linear unloading region under infinitely large strain, $A_{\text{an}} - B_{\text{an}}$ is the initial size of the linear unloading region, η_{an} is the material parameter determined from measured loading and unloading stress-strain curves.

In the presented model, the linear and nonlinear unloading modulus can be given from Eqs. (6) and (7). In the QPE model, the linear unloading modulus E_{lu} is the initial elastic modulus E_0, and the nonlinear unloading modulus E_{nu} can be obtained from Eq. (4).

4.2 Constitutive model

To distinguish linear elastic and anelastic behaviors, the anelastic surface (see Fig. 7b) is defined in a three-dimensional (3-D) stress space as follows:

$$f_{\text{an}} = \phi_{\text{an}}(\boldsymbol{\sigma} - \boldsymbol{\alpha}_{\text{an}}) - R_{\text{an}}(p) = 0, \tag{10}$$

where ϕ_{an} is the anelastic surface function, $\boldsymbol{\sigma}$ is the stress tensor, R_{an} is the size of the anelastic surface, $\boldsymbol{\alpha}_{\text{an}}$ is the center of the anelastic surface. Moreover, the yield surface represents a transition from elastic or anelastic behavior to plastic elastic can be expressed as

$$f_y = \phi_y(\boldsymbol{\sigma}_y - \boldsymbol{\alpha}_y) - R_y(p) = 0, \tag{11}$$

where ϕ_y is the yield surface function, $\boldsymbol{\sigma}_y$ is the stress tensor, R_y represents the size of the yield surface, and the tensor $\boldsymbol{\alpha}_y$ is the center of the yield surface. The variable p is the equivalent plastic strain, which can be given from von Mises yield functions:

$$\mathrm{d}p = \left(\frac{2}{3}\mathrm{d}\boldsymbol{\varepsilon}_{\text{p}} : \mathrm{d}\boldsymbol{\varepsilon}_{\text{p}}\right)^{1/2}. \tag{12}$$

According to anelastic surface and yield surface, a stress point can only lie in a linear elastic state, anelastic state, or plastic state.

4.2.1 *Linear elastic state*

In the linear elastic state, $\boldsymbol{\sigma}$ is inside or on the anelastic surface and the normal to the surface at the loading point projecting inward. The sizes and centers of f_{an} and f_y are unchanged. Only elastic strain $\boldsymbol{\varepsilon}_{\text{e}}$ occurs, and the governing equations are thus as follows:

$$\mathrm{d}\boldsymbol{\varepsilon} = \mathrm{d}\boldsymbol{\varepsilon}_{\text{e}}, \tag{13}$$

$$\mathrm{d}\boldsymbol{\sigma} = \mathbf{C}_{\text{e}} : \mathrm{d}\boldsymbol{\varepsilon}_{\text{e}}, \tag{14}$$

where $\mathbf{C}_{\text{e}}$ is the elastic stiffness tensor, and the elastic modulus can be obtained from Eq. (6).

4.2.2 *Plastic state*

In the plastic state, $\boldsymbol{\sigma}$ is on the yield surface with its increment $\mathrm{d}\boldsymbol{\sigma}$ projecting outward, and the anelastic surface is coincident with the yield surface when $\boldsymbol{\sigma} = \boldsymbol{\sigma}_y$. In this state, both elastic strain ε_{e}, anelastic strain $\boldsymbol{\varepsilon}_{\text{an}}$ and plastic strain $\boldsymbol{\varepsilon}_{\text{p}}$ will occur. The governing equations are as follows:

$$\mathrm{d}\boldsymbol{\varepsilon} = \mathrm{d}\boldsymbol{\varepsilon}_{\text{e}} + \mathrm{d}\boldsymbol{\varepsilon}_{\text{an}} + \mathrm{d}\boldsymbol{\varepsilon}_{\text{p}}, \tag{15}$$

$$\mathrm{d}\boldsymbol{\sigma} = \mathbf{C}_{\text{e}} : \mathrm{d}\boldsymbol{\varepsilon}_{\text{e}} = \mathbf{C}_{\text{p}} : \mathrm{d}\boldsymbol{\varepsilon}_{\text{p}}, \tag{16}$$

where $\mathbf{C}_{\text{p}}$ is the apparent elasticity tensor at plastic state, and can be calculated as

$$\mathbf{C}_{\text{p}} = \frac{E_{\text{chord}}}{E_0}\mathbf{C}_{\text{e}}, \tag{17}$$

where E_{chord} can be obtained from Eq. (3).

Zang's model [62] described the plastic hardening behavior, revealing the relationship between flow stress and equivalent plastic strain:

$$R_y(p) = \sigma_{y0} + Q_y\left[1 - \exp\left(-b_y \cdot p\right)\right] + C_y \cdot p. \tag{18}$$

Therefore, the evolution of the yield surface can be written as

$$\mathrm{d}R_y(p) = b_y Q_y \exp\left(-b_y \cdot p\right)\mathrm{d}p + C_y, \tag{19}$$

where σ_{y0} is the initial size of the yield surface, and Q_y, b_y and C_y are material parameters determined from loading and unloading stress-strain curves, respectively.

According to plastic flow rules, the equivalent plastic strain increment can be expressed as

$$\mathrm{d}\boldsymbol{\varepsilon}_{\text{p}} = \mathrm{d}\lambda\frac{\partial f_y}{\partial \boldsymbol{\sigma}}, \tag{20}$$

where $\mathrm{d}\lambda$ is the plastic multiplier, which is defined as $\mathrm{d}\lambda = \mathrm{d}p$.

4.2.3 *Anelastic state*

In the anelastic state, $\boldsymbol{\sigma}$ is on the anelastic surface with its increment $\mathrm{d}\boldsymbol{\sigma}$ projecting outward but not in contact with the yield surface. In this state, the anelastic surface moves towards the yield surface. The center of f_y and the size of f_{an} are unchanged, and both elastic strain $\boldsymbol{\varepsilon}_{\text{e}}$ and anelastic strain $\boldsymbol{\varepsilon}_{\text{an}}$ will occur. The governing equations are as follows:

$$\mathrm{d}\boldsymbol{\varepsilon} = \mathrm{d}\boldsymbol{\varepsilon}_{\text{e}} + \mathrm{d}\boldsymbol{\varepsilon}_{\text{an}}, \tag{21}$$

$$\mathrm{d}\boldsymbol{\sigma} = \mathbf{C}_{\text{e}} : \mathrm{d}\boldsymbol{\varepsilon}_{\text{e}} = \mathbf{C}_{\text{an}} : \mathrm{d}\boldsymbol{\varepsilon}, \tag{22}$$

$$\mathrm{d}\boldsymbol{\alpha}_{\text{an}} = \frac{\mathbf{n}_{\text{an}} : \mathrm{d}\boldsymbol{\sigma}}{\mathbf{n}_{\text{an}} : (\boldsymbol{\sigma}_y - \boldsymbol{\sigma})}(\boldsymbol{\sigma}_y - \boldsymbol{\sigma}), \tag{23}$$

where $\mathbf{C}_{\text{an}}$ is an apparent elastic + an elastic stiffness tensor, and can be written as

$$\mathbf{C}_{\text{an}} = \frac{E_{\text{nu}}}{E_0}\mathbf{C}_{\text{e}}, \tag{24}$$

where E_{nu} can be obtained from Eq. (7).

The constitutive equation of the quantitative model can be implemented into ABAQUS/Standard 6.14 using the user subroutines UMAT [63], and the algorithm and numerical procedures were described in Refs. [38,64]. Therefore, the Nb_3Sn superconducting composite wires FE model has been constructed with 2976 nodes and 2397 C3D8I elements after mesh sizes and convergence analysis (see Fig. 8). The paraments for the present model and QPE model were fitted in Sect. 2 of Appendix.

5. Damage evolution model for fatigue processes

To relate the damage degradation and energy dissipation for the fatigue process, a damage evolution model has been conducted. Based on the stiffness degradation rule of composites [65], the damage factors of matrix and fiber can be defined as

$$D(N) = \frac{E_0 - E(N)}{E_0 - E_f}, \tag{25}$$

where E_0 is the initial chord modulus; E_f is the chord modulus at failure; and $E(N)$ is the chord modulus during fatigue process.

Generally, Lemaitre's plastic damage model [60] has been

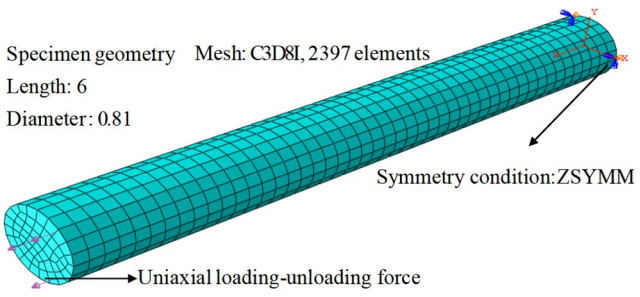

Figure 8 Nb_3Sn superconducting composite wires FE model.

widely used for damage evolution analysis, which can be expressed as

$$\frac{\mathrm{d}D(N)}{\mathrm{d}N}=\frac{\left[\Delta\sigma(N)\right]^2}{2\left[1-D(N)\right]^2E_0S}\Delta\varepsilon_{\mathrm{p}}(N), \tag{26}$$

where $\Delta\varepsilon_p(N)$ is the plastic strain range, $\Delta\sigma(N)$ is stress range, and S is the energy strength of damage. A cyclic relationship between $\Delta\sigma(N)$ and $\Delta\varepsilon_{\mathrm{p}}(N)$ [66] can be written as

$$\Delta\varepsilon_{\mathrm{p}}(N)=\left[\frac{\Delta\sigma(N)}{K(1-D)}\right]^M, \tag{27}$$

where K and M are the model parameters. Substituting Eq. (27) into Eq. (26) yields

$$\frac{\mathrm{d}D(N)}{\mathrm{d}N}=\frac{K^2}{2E_0S}\left[\Delta\varepsilon_p(N)\right]^{\frac{M+2}{M}}. \tag{28}$$

The energy dissipation is caused by plastic accumulation, and the common form is usually characterized by a stress-strain hysteresis loop area at one fatigue cycle [67], which can be written as

$$\Delta W(N)=\frac{1-\frac{1}{M}}{1+\frac{1}{M}}K\left[\Delta\varepsilon_{\mathrm{p}}(N)\right]^{1+\frac{1}{M}}. \tag{29}$$

Substituting Eq. (29) into Eq. (28), the relationship between energy dissipation and damage can be obtained as

$$\frac{\mathrm{d}D(N)}{\mathrm{d}N}=\frac{K^2}{2E_0S}\left[\frac{M+1}{(M-1)K}\right]^{\frac{M+2}{1+M}}\left[\Delta W(N)\right]^{\frac{M+2}{1+M}}. \tag{30}$$

The Nb_3Sn superconducting composite wires exhibit three fatigue stages, namely, initially rapid damage, steady damage, and accelerated damage stages [52]. The three-parameter damage model considering the degradation of Cu matrix and Nb_3Sn sub-elements has been derived in previous work [52], which can be written as

$$D(N)=q\left(\frac{N}{N_f}\right)^{m_m}+(1-q)\left(\frac{N}{N_f}\right)^{m_f}, \tag{31}$$

where q, m_m and m_f is material parameters related to the interfacial strength and volume fraction of each constituent.

Substituting Eq. (31) into Eq. (30), the energy dissipation can be obtained as

$$\Delta W(N)=\frac{(M-1)K}{\mathrm{M}+1}\left[\frac{K^2}{2E_0S}\right]^{-\frac{2+M}{1+M}}\cdot\left[q\frac{m_m}{N_f}\left(\frac{N}{N_f}\right)^{m_m-1}+(1-q)\frac{m_f}{N_f}\left(\frac{N}{N_f}\right)^{m_f-1}\right]^{\frac{2+M}{1+M}}. \tag{32}$$

Then, Eq. (32) also can be simplified as

$$\Delta W(N)=A\left[q\frac{m_m}{N_f}\left(\frac{N}{N_f}\right)^{m_m-1}+(1-q)\frac{m_f}{N_f}\left(\frac{N}{N_f}\right)^{m_f-1}\right]^B. \tag{33}$$

Here, the parameters A and B are expressed as follows:

$$A=\frac{(M-1)K}{\mathrm{M}+1}\left[\frac{K^2}{2E_0S}\right]^{-\frac{2+M}{1+M}}, \tag{34}$$

$$B=\frac{2+M}{1+M}. \tag{35}$$

When Nb_3Sn superconducting composite wires occur to fatigue failure, the energy dissipation at one cycle is defined as critical energy dissipation ΔW_f. In this paper, the critical energy dissipation ΔW_f can be obtained from experimental data.

When $N=N_f$ and $\Delta W(N)=\Delta W_f$, $\Delta W(N)$ can be derived as

$$\Delta W(N)=\Delta W_f\left[\frac{q\frac{m_m}{N_f}\left(\frac{N}{N_f}\right)^{m_m-1}+(1-q)\frac{m_f}{N_f}\left(\frac{N}{N_f}\right)^{m_f-1}}{q\frac{m_m}{N_f}+(1-q)\frac{m_f}{N_f}}\right]^B. \tag{36}$$

Therefore, the energy dissipation considering damage evolution of Nb_3Sn superconducting composite wires can be solved by Eq. (36) during fatigue tests with the temperature of 77 and 300 K. The paraments for Eq. (36) were fitted in Sect. 3 of Appendix.

6. Discussion

6.1 Quasi-static theoretical prediction

The stress-strain hysteresis curves and energy dissipation of the theoretical models and experimental results are shown in Fig. 9 with the temperature of 77 and 300 K. Our theoretical model results show that the stress-strain hysteresis curves and energy dissipation are in good agreement with experimental data, and are more accurate than the QPE model at the temperature of 77 and 300 K. The energy dissipation errors of the presented model and QPE model are displayed in Fig. 9c and f. It can be seen that, at 77 K, the energy dissipation errors of the presented model are between −5.97% and 3.72%, while that of the QPE model are between −15.8% and 81.5% (see Fig. 9c). When the temperature of 300 K, the energy dissipation errors are between −6.28% and 2.13%, which are much less than that of QPE model, about −58.0% and 38.3% (see Fig. 9f). Therefore, our theoretical model can more accurately predict energy dissipation at various temperatures.

With the increase of unloading stress, energy dissipations obtained by the presented model and experimental results show nonlinearity, but that of the QPE model show linearity, which indicated that nonlinearities of the energy dissipation for Nb_3Sn superconducting composite wires are mainly caused by fatigue damage.

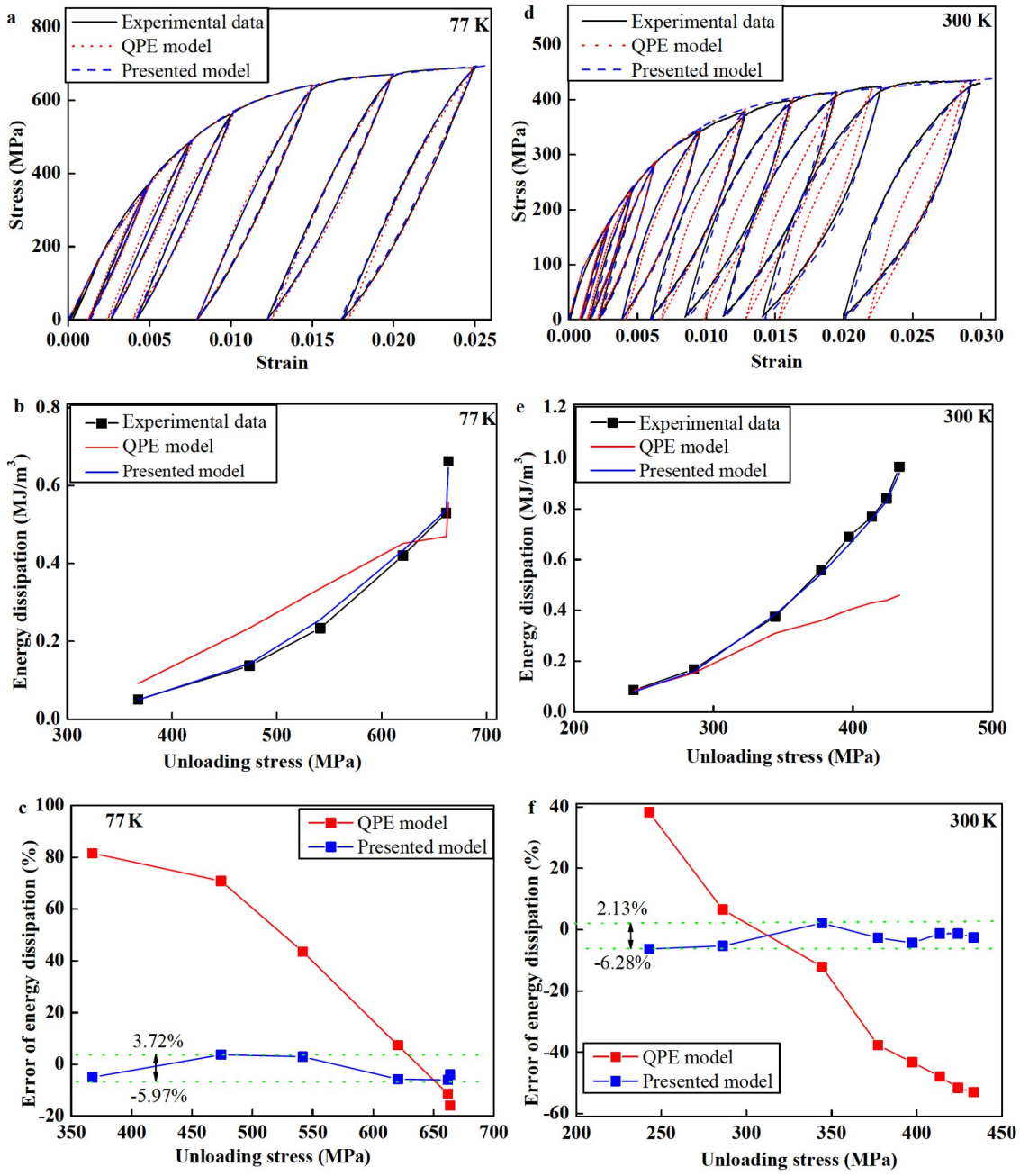

Figure 9 Comparison of nonlinearity between the theoretical model results and experimental data with various temperatures. **a-c** 77 K; **d-f** 300 K.

6.2 Energy dissipation of fatigue tests

The energy dissipation for Nb_3Sn superconducting composite wires with various strain ranges is shown in Fig. 10. It can be seen that the predicted results are in agreement with the experimental results. Therefore, the theoretical model Eq. (36) can predict the energy dissipation for Nb_3Sn superconducting composite wire at the temperature of 77 and 300 K, which can exhibit the advantage of energy dissipation derived from damage degradation, and solve the different forms of energy dissipation. For superconducting materials, large temperature change due to energy dissipation may cause quench, thermal strain and microscale damage [19,68].

6.3 Nonlinearity of quasi-static stress-strain responses

Anelastic strain is the nonlinear term in the unloading process (see Fig. 7). The ratio of anelastic and elastic strain can evaluate the strength in the nonlinearity of unloading-reloading stress-strain responses, which is positively correlated with the nonlinearity of unloading-reloading stress-

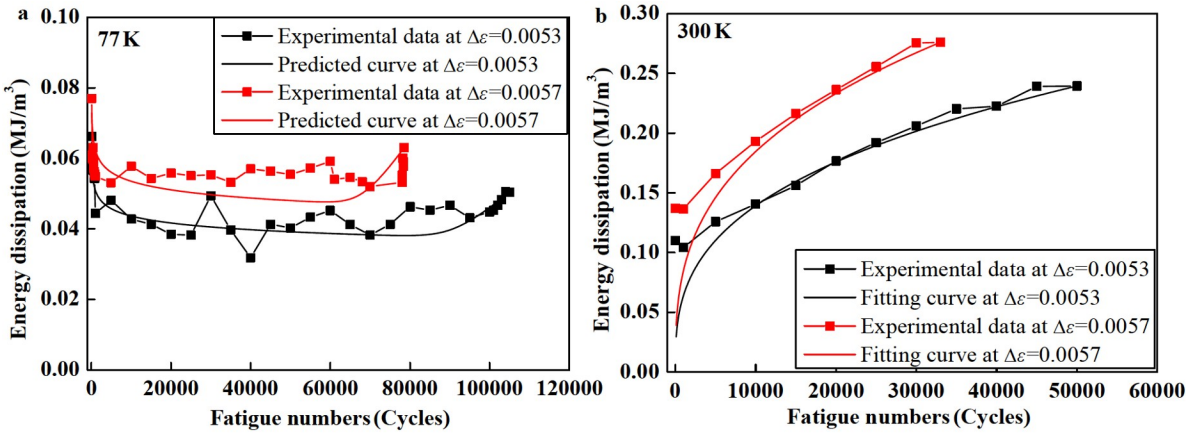

Figure 10 The energy dissipation of Nb_3Sn superconducting composite wires with various strain ranges at the temperature of **a** 77 K, and **b** 300 K.

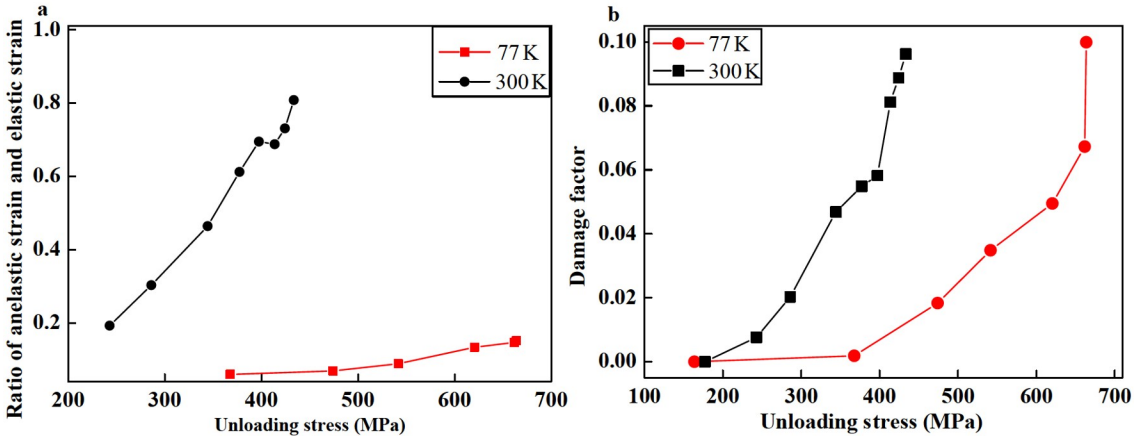

Figure 11 The comparison of the nonlinearity at 77 K and 300 K. **a** The ratio of anelastic strain and elastic strain; **b** the damage factor.

strain responses. When this ratio is zero, the unloading processes are linear unloading. For Nb_3Sn superconducting composite wires, the ratio of anelastic and elastic strain can be obtained from Fig. 3, as shown in Fig. 11a. It can be seen that the ratio of anelastic and elastic strain at 300 K is larger than at 77 K due to the Nb_3Sn superconducting composite wires are brittle at 77 K. Then, the ratio in Nb_3Sn superconducting composite wires nonlinearly increases with unloading stress, which is different from that of the low-strength, bake-hardenable and advanced high-strength steels [38,39], where the ratio of anelastic and elastic strain is a linear relationship with unloading stress. Moreover, the increasing speed of the ratio is larger at 300 K than 77 K, which is linked with the damage (see Fig. 11b). In Fig. 11b, the damage increases with unloading stress, and is larger at 300 K than 77 K.

6.4 Analyses of the fracture modes

Figure 12a and d illustrates the fracture surface of Nb_3Sn superconducting composite wires after fatigue testing at a strain range of 0.005. The results show that where fracture surfaces show typical fracture characteristics with three regions of fatigue source, propagation zone and final rupture region marked by the red arrows. Moreover, the fracture surface of Nb_3Sn superconducting composite wires at 300 K fatigue is rougher than at 77 K, and the phenomena indicate that Nb_3Sn superconducting composite wires need to overcome larger dislocations and generate larger energy dissipation at 300 K, which is in agreement with the results in Fig. 6.

The Nb_3Sn sub-element of position 1 in fracture surface at 77 and 300 K are fatigue sources, shown in Fig. 12b and e, and fatigue source sites could be identified by tracking the river-like patterns [69]. The positions of fatigue sources are close to the diffusion barrier, because the outside of the diffusion barrier is the Cu matrix, and the outside of the diffusion barrier is the Nb_3Sn sub-elements, which can cause obvious stress concentration. A closer examination reveals that there are interface debonding and inter-Nb_3Sn cracking at the fatigue source in Fig. 12b and e. From the results, the fatigue source is caused by interface debonding

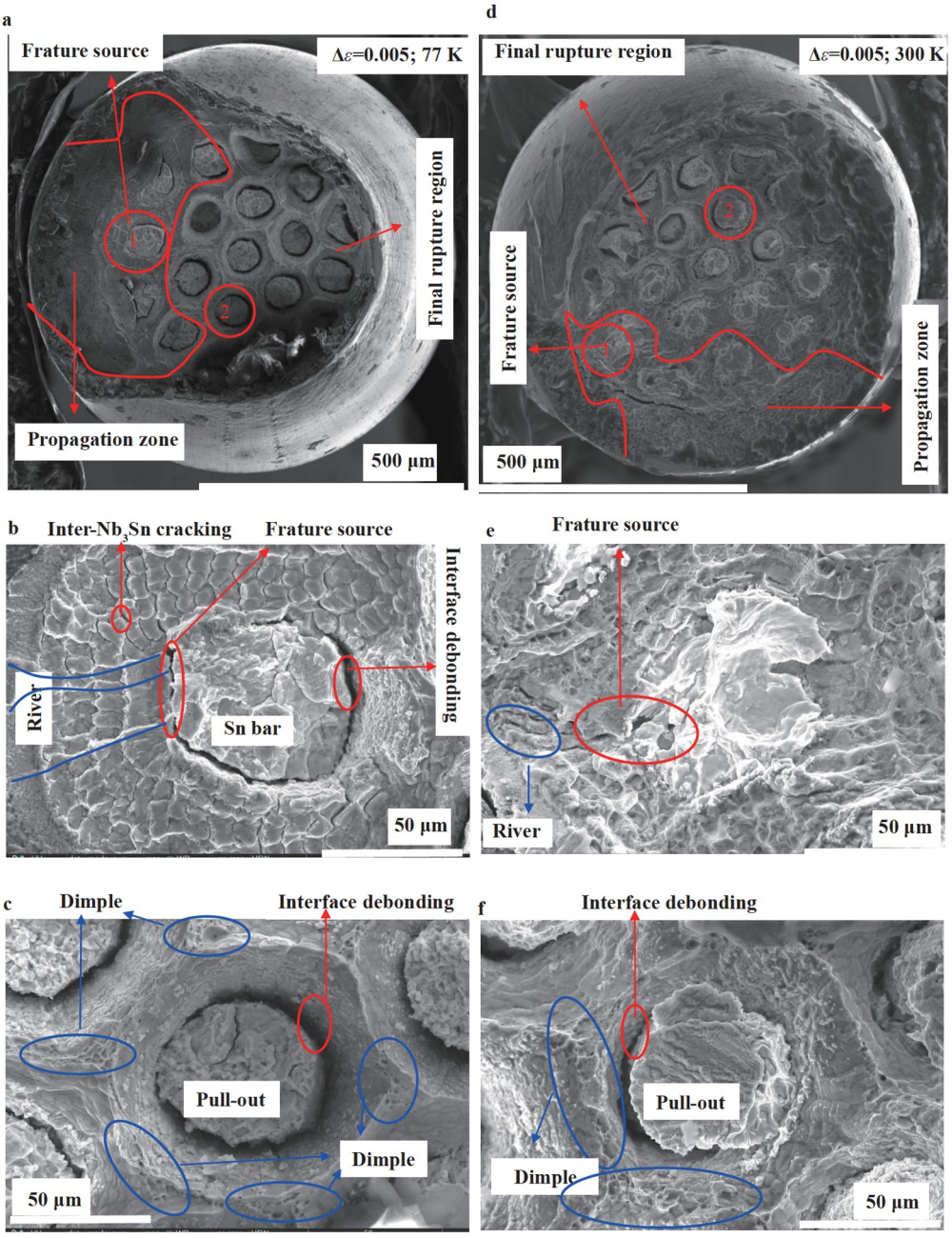

Figure 12 The fracture morphologies of Nb_3Sn superconducting composite wires during fatigue tests. **a** Fracture surface at 77 K; **b** Nb_3Sn sub-element of position 1 at Fig. 12a; **c** Nb_3Sn sub-element of position 2 at Fig. 12a; **d** fracture surface at 300 K; **e** Nb_3Sn sub-element of position 1 at Fig. 12d; **f** Nb_3Sn sub-element of position 2 at Fig. 12d.

at 77 K, and is caused by Nb_3Sn sub-element cracking at 300 K. From Fig. 12b and e, the fatigue failure of Nb_3Sn sub-elements is brittle fracture at 77 K, and ductile fracture at 300 K.

The Nb_3Sn sub-element of position 2 in Fig. 12a and d are in the region at the end of fatigue, shown in Fig. 12c and f, where there are Sn bar pull-out, interface debonding and lots of dimples. At the end of fatigue, void nucleation and growth can cause lots of dimples in ductile metal, and dimples can be used to judge the final rupture region. In Fig. 12a and d, at the propagation zone, cracks grow stably, and the zone is essentially flat.

7. Conclusions

In this work, the nonlinear mechanical behaviors of Nb_3Sn superconducting composite wire have been investigated by experimental tests and theoretical analysis, such as the quasi-static loading-unloading stress-strain curves, energy

dissipation and fatigue at 77 and 300 K. The main conclusions can be summarized as follows.

The energy dissipations exhibit strong nonlinearity with unloading stress during the quasi-static loading-unloading process. After considering damage degradation, the new elastic-plastic constitutive model can accurately predict the quasi-static loading-unloading stress-strain responses and energy dissipation. According to the comparisons of the present model and QPE model, damage degradation can be considered as the main reason for the nonlinearity of energy dissipation.

The energy dissipations present two different modes at room temperature and liquid nitrogen during fatigue tests. At the temperature of 77 K, the energy dissipations show three stages: initial rapid drop, steady stage and accelerated increase, while at 300 K, they gradually increase with fatigue cycles. A new fatigue model based on the damage has been conducted, which can accurately predict the energy dissipations not only at room temperature but also at liquid nitrogen.

There are three typical fracture regions of Nb_3Sn composite wire whether 77 or 300 K: fatigue source, propagation zone and final rupture region. The positions of fatigue sources in Nb_3Sn sub-elements are close to the diffusion barrier. Fatigue cracks grow from the fatigue sources inside of the diffusion barrier, through the diffusion barrier, and extend to the Cu matrix until the strand breaks. Moreover, the fatigue source at 77 K is caused by interface debonding, while it is caused by Nb_3Sn sub-element cracking at 300 K. The fatigue failure of Nb_3Sn/Cu sub-elements is a brittle fracture at 77 K, and ductile fracture at 300 K.

Author contributions *You-He Zhou and Xingyi Zhang designed the research. Lang Jiang wrote the first draft of the manuscript, set up the experiment set-up and processed the experiment data. Xingyi Zhang helped organize the manuscript, and revised and edited the final version.*

Acknowledgements *This work was supported by the National Natural Science Foundation of China (Grant Nos. 11872196, 12232005 and U2241267).*

1 E. Gibney, Fuel for world's largest fusion reactor ITER is set for test run, Nature **591**, 15 (2021).
2 Neutrino hunt resumes, ITER's new confidence and Elsevier's woes, Nature **566**, 12 (2019).
3 M. Breschi, D. Macioce, and A. Devred, Performance analysis of the toroidal field ITER production conductors, Supercond. Sci. Technol. **30**, 055007 (2017).
4 X. Xiao, D. Terentyev, H. Chu, and H. Duan, Theoretical models for irradiation hardening and embrittlement in nuclear structural materials: A review and perspective, Acta Mech. Sin. **36**, 397 (2020).
5 J. Qin, Y. Wu, J. Li, F. Liu, C. Dai, Y. Shi, H. Liu, Z. Mao, A. Nijhuis, C. Zhou, K. A. Yagotintsev, R. Lubkemann, V. A. Anvar, and A. Devred, New design of cable-in-conduit conductor for application in future fusion reactors, Supercond. Sci. Technol. **30**, 115012 (2017).
6 Z. Guo, C. Dai, J. Qin, C. Zhou, J. Li, W. Yu, F. Liu, D. Yang, C. Huang, L. Li, H. Zhang, T. Xue, A. Nijhuis, and A. Devred, Research on mechanical properties of high-performance cable-in-conduit conductors with different design, Supercond. Sci. Technol. **33**, 045002 (2020).
7 G. De Marzi, B. Bordini, and D. Baffari, On the mechanisms governing the critical current reduction in Nb_3Sn Rutherford cables under transverse stress, Sci. Rep. **11**, 1 (2021).
8 G. Brumfiel, Cable test raises fears at fusion project, Nature **471**, 150 (2011).
9 Y. He, Z. Shi, L. Qiao, G. Xiao, Z. Li, and L. Yang, Electromechanical coupling in high-pressured superconducting Nb_3Sn: Analytical and simulation models, Int. J. Mech. Sci. **230**, 107541 (2022).
10 A. Godeke, A review of the properties of Nb_3 Sn and their variation with A15 composition, morphology and strain state, Supercond. Sci. Technol. **19**, R68 (2006).
11 W. D. Markiewicz, Comparison of strain scaling functions for the strain dependence of composite Nb_3Sn superconductors, Supercond. Sci. Technol. **21**, 054004 (2008).
12 J. E. Duvauchelle, B. Bordini, J. Fleiter, and A. Ballarino, Critical current measurements under transverse pressure of a Nb_3 Sn Rutherford cable based on 1 mm RRP wires, IEEE Trans. Appl. Supercond. **28**, 1 (2018).
13 L. Gämperle, J. Ferradas, C. Barth, B. Bordini, D. Tommasini, and C. Senatore, Determination of the electromechanical limits of high-performance Nb_3Sn Rutherford cables under transverse stress from a single-wire experiment, Phys. Rev. Res. **2**, 013211 (2020).
14 G. De Marzi, V. Corato, L. Muzzi, A. della Corte, G. Mondonico, B. Seeber, and C. Senatore, Reversible stress-induced anomalies in the strain function of Nb_3 Sn wires, Supercond. Sci. Technol. **25**, 025015 (2012).
15 B. Seeber, C. Calzolaio, D. Zurmühle, V. Abächerli, M. Alessandrini, G. De Marzi, and C. Senatore, Reduced strain sensitivity of the critical current of Nb_3 Sn multifilamentary wires, J. Appl. Phys. **126**, 203905 (2019).
16 G. Xiao, H. Jin, C. Zhou, H. Ma, D. Wang, F. Liu, H. Liu, A. Nijhuis, and A. Devred, Performance of highly flexible sub-cable for REBCO cable-in-conduit conductor at 5.8 T applied field, Superconductivity **3**, 100023 (2022).
17 N. N. Martovetsky, P. Bruzzone, B. Stepanov, R. Wesche, C. Gung, J. V. Minervini, M. Takayasu, L. F. Goodrich, J. W. Ekin, and A. Nijhuis, Effect of conduit material on CICC performance under high cycling loads, IEEE Trans. Appl. Supercond. **15**, 1367 (2005).
18 P. Bruzzone, A. M. Fuchs, B. Stepanov, and G. Vecsey, Performance evolution of Nb_3Sn cable-in-conduit conductors under cyclic load [for Tokamaks], IEEE Trans. Appl. Supercond. **12**, 516 (2002).
19 N. Martovetsky, P. Michael, J. Minervini, A. Radovinsky, M. Takayasu, C. Y. Gung, R. Thome, T. Ando, T. Isono, K. Hamada, T. Kato, K. Kawano, N. Koizumi, K. Matsui, H. Nakajima, G. Nishijima, Y. Nunoya, M. Sugimoto, Y. Takahashi, H. Tsuji, D. Bessette, K. Okuno, N. Mitchell, M. Ricci, R. Zanino, L. Savoldi, K. Arai, and A. Ninomiya, Test of the ITER central solenoid model coil and CS insert, IEEE Trans. Appl. Supercond. **12**, 600 (2002).
20 C. Sanabria, P. J. Lee, W. Starch, T. Blum, A. Devred, M. C. Jewell, I. Pong, N. Martovetsky, and D. C. Larbalestier, Metallographic autopsies of full-scale ITER prototype cable-in-conduit conductors after full testing in SULTAN: 1. The mechanical role of copper strands in a CICC, Supercond. Sci. Technol. **28**, 085005 (2015).
21 D. Yue, X. Zhang, and Y. H. Zhou, Theoretical analysis for the mechanical behavior caused by an electromagnetic cycle in ITER Nb_3 Sn cable-in-conduit conductors, Acta Mech. Sin. **34**, 614 (2018).
22 J. Tabin, B. Skoczeń, and J. Bielski, Discontinuous plastic flow in superconducting multifilament composites, Int. J. Solids Struct. **202**, 12 (2020).
23 E. Q. Sun, Multi-scale nonlinear stress analysis of Nb_3 Sn superconducting accelerator magnets, Supercond. Sci. Technol. **35**, 045019 (2022).

24 W. Prager, A new method of analyzing stresses and strains in work-hardening plastic solids, J. Appl. Mech. **23**, 493 (1956).
25 H. Ziegler, A modification of Prager's hardening rule, Appl. Math. **17**, 55 (1959).
26 P. J. Armstrong, and C. O. Frederick, A mathematical representation of the multiaxial Bauschinger effect, Mater. High Temp. **24**, 1 (1966).
27 J. L. Chaboche, Time-independent constitutive theories for cyclic plasticity, Int. J. Plast. **2**, 149 (1986).
28 F. Yoshida, and T. Uemori, A model of large-strain cyclic plasticity and its application to springback simulation, Int. J. Mech. Sci. **45**, 1687 (2003).
29 F. Yoshida, and T. Uemori, A model of large-strain cyclic plasticity describing the Bauschinger effect and workhardening stagnation, Int. J. Plast. **18**, 661 (2002).
30 M. Lee, D. Kim, C. Kim, M. Wenner, R. Wagoner, and K. Chung, A practical two-surface plasticity model and its application to spring-back prediction, Int. J. Plast. **23**, 1189 (2007).
31 J. Y. Lee, M. G. Lee, F. Barlat, and G. Bae, Piecewise linear approximation of nonlinear unloading-reloading behaviors using a multi-surface approach, Int. J. Plast. **93**, 112 (2017).
32 D. C. Pham, Consistent limited kinematic hardening plasticity theory and path-independent shakedown theorems, Int. J. Mech. Sci. **130**, 11 (2017).
33 D. Weichert, and J. Gross-Weege, The numerical assessment of elastic-plastic sheets under variable mechanical and thermal loads using a simplified two-surface yield condition, Int. J. Mech. Sci. **30**, 757 (1988).
34 A. Ghaei, and D. E. Green, Numerical implementation of Yoshida-Uemori two-surface plasticity model using a fully implicit integration scheme, Comput. Mater. Sci. **48**, 195 (2010).
35 A. Ghaei, and A. Taherizadeh, A two-surface hardening plasticity model based on non-associated flow rule for anisotropic metals subjected to cyclic loading, Int. J. Mech. Sci. **92**, 24 (2015).
36 L. J. Jia, Integration algorithm for a modified Yoshida-Uemori model to simulate cyclic plasticity in extremely large plastic strain ranges up to fracture, Comput. Struct. **145**, 36 (2014).
37 H. Hajbarati, and A. Zajkani, A novel analytical model to predict springback of DP780 steel based on modified Yoshida-Uemori two-surface hardening model, Int. J. Mater. Form. **12**, 441 (2019).
38 L. Sun, and R. H. Wagoner, Complex unloading behavior: Nature of the deformation and its consistent constitutive representation, Int. J. Plast. **27**, 1126 (2011).
39 J. Lee, J. Y. Lee, F. Barlat, R. H. Wagoner, K. Chung, and M. G. Lee, Extension of quasi-plastic-elastic approach to incorporate complex plastic flow behavior—application to springback of advanced high-strength steels, Int. J. Plast. **45**, 140 (2013).
40 E. H. Lee, T. B. Stoughton, and J. W. Yoon, A new strategy to describe nonlinear elastic and asymmetric plastic behaviors with one yield surface, Int. J. Plast. **98**, 217 (2017).
41 H. Hou, G. Zhao, L. Chen, and H. Li, Springback behavior and a new chord modulus model of copper alloy during severe plastic compressive deformation, J. Mater. Process. Tech. **290**, 116974 (2021).
42 N. C. van den Eijnden, A. Nijhuis, Y. Ilyin, W. A. J. Wessel, and H. H. J. ten Kate, Axial tensile stress-strain characterization of ITER model coil type Nb_3 Sn strands in TARSIS, Supercond. Sci. Technol. **18**, 1523 (2005).
43 K. Osamura, S. Machiya, Y. Tsuchiya, H. Suzuki, T. Shobu, M. Sato, T. Hemmi, Y. Nunoya, and S. Ochiai, Local strain and its influence on mechanical-electromagnetic properties of twisted and untwisted ITER Nb_3 Sn strands, Supercond. Sci. Technol. **25**, 054010 (2012).
44 A. Nijhuis, R. P. Pompe van Meerdervoort, H. J. G. Krooshoop, W. A. J. Wessel, C. Zhou, G. Rolando, C. Sanabria, P. J. Lee, D. C. Larbalestier, A. Devred, A. Vostner, N. Mitchell, Y. Takahashi, Y. Nabara, T. Boutboul, V. Tronza, S. H. Park, and W. Yu, The effect of axial and transverse loading on the transport properties of ITER Nb_3 Sn strands, Supercond. Sci. Technol. **26**, 084004 (2013).
45 A. Nijhuis, Mechanical and Electro-Magnetic Performance of Nb_3Sn Superconductors for Fusion, Dissertation for Doctoral Degree (University of Twente, Enschede, 2016).
46 G. Lenoir, P. Manil, F. Nunio, and V. Aubin, Mechanical behavior laws for multiscale numerical model of Nb_3 Sn conductors, IEEE Trans. Appl. Supercond. **29**, 1 (2019).
47 H. Bajas, Numerical Simulation of the Mechanical Behavior of the ITER Cable-In-Conduit Conductors, Dissertation for Doctoral Degree (Ecole Centrale de Paris, Paris, 2011).
48 W. Du, D. Wang, and Y. Zhou, Establishment of 3D multistage models of superconducting cable based on discrete element method, Supercond. Sci. Technol. **34**, 085017 (2021).
49 X. Wang, Y. Li, and Y. Gao, Mechanical behaviors of multi-filament twist superconducting strand under tensile and cyclic loading, Cryogenics **73**, 14 (2016).
50 S. F. Cogan, and R. M. Rose, Fatigue effects in unidirectional composites: Applications to Nb_3 Sn superconductors, Appl. Phys. Lett. **35**, 884 (1979).
51 R. Riccioli, Mechanical Modelling of Superconducting Cables for Fusion under Cyclic Electromagnetic and Thermal Loads, Dissertation for Doctoral Degree (University of Bologna, Bologna, 2021).
52 L. Jiang, X. Su, L. Shen, J. Zhou, and X. Zhang, Damage behavior of Nb_3Sn/Cu superconducting strand at room temperature under asymmetric strain cycling, Fusion Eng. Des. **172**, 112869 (2021).
53 A. Vostner, and E. Salpietro, Enhanced critical current densities in Nb_3 Sn superconductors for large magnets, Supercond. Sci. Technol. **19**, S90 (2006).
54 C. G. Li, C. J. Xiao, J. Q. Guan, X. G. Sun, J. W. Liu, X. H. Liu, Y. Feng, P. X. Zhang, and J. S. Li, Investigation of superconducting properties of Nb_3Sn strands by internal tin process for ITER, IEEE Trans. Appl. Supercond. **20**, 1484 (2010).
55 A. Torkabadi, E. S. Perdahcıoğlu, V. T. Meinders, and A. H. van den Boogaard, On the nonlinear anelastic behavior of AHSS, Int. J. Solids Struct. **151**, 2 (2018).
56 C. S. Grimmer, and C. K. H. Dharan, High-cycle fatigue of hybrid carbon nanotube/glass fiber/polymer composites, J. Mater. Sci. **43**, 4487 (2008).
57 N. Mitchell, Finite element simulations of elasto-plastic processes in Nb_3Sn strands, Cryogenics **45**, 501 (2005).
58 J. L. Chaboche, Continuum damage mechanics: Part I—General concepts, J. Appl. Mech. **55**, 59 (1988).
59 J. L. Chaboche, Continuum damage mechanics: Part II—Damage growth, crack initiation, and crack growth, J. Appl. Mech. **55**, 65 (1988).
60 J. Lemaitre, A Course on Damage Mechanics (Springer Science & Business Media, Berlin/Heidelberg, 2012).
61 F. Yoshida, T. Uemori, and K. Fujiwara, Elastic-plastic behavior of steel sheets under in-plane cyclic tension-compression at large strain, Int. J. Plast. **18**, 633 (2002).
62 M. Safaei, S. Zang, M. G. Lee, and W. De Waele, Evaluation of anisotropic constitutive models: Mixed anisotropic hardening and non-associated flow rule approach, Int. J. Mech. Sci. **73**, 53 (2013).
63 D. Systèmes, Abaqus User Subroutines Reference Guide, Version 6.14 (Dassault Systemes Simulia Corp, Providence, 2014).
64 X. Feng, Y. P. Yao, R. N. Li, Z. Wan, and X. Dai, Loading-unloading judgement for advanced plastic UH model, Acta Mech. Sin. **36**, 827 (2020).
65 F. Wu, and W. X. Yao, A fatigue damage model of composite materials, Int. J. Fatigue **32**, 134 (2010).
66 J. Lemaitre, and R. Desmorat, Engineering Damage Mechanics: Ductile, Creep, Fatigue and Brittle Failures (Springer Science & Business Media, Berlin/Heidelberg, 2005).
67 V. Kliman, and M. Bílý, Hysteresis energy of cyclic loading, Mater. Sci. Eng. **68**, 11 (1984).
68 Z. Jing, and M. D. Ainslie, Numerical simulation of flux avalanches

in type-II superconducting thin films under transient AC magnetic fields, Supercond. Sci. Technol. **33**, 084006 (2020).
69 F. Han, C. Liu, F. Yuan, Y. Zhang, M. Ali, H. Gu, and G. Li, Microscopic characterization on low cycle fatigue behavior at room temperature of Zircaloy-4 alloy with recrystallized microstructure, J. Alloys Compd. **778**, 318 (2019).

Nb_3Sn超导复合股线非线性力学行为研究

姜浪, 张兴义, 周又和

摘要 本文通过对Nb_3Sn超导复合股线在77 K和300 K下进行准静态加卸载拉伸和疲劳实验, 研究了Nb_3Sn超导复合股线的非线性力学行为, 结果表明: Nb_3Sn超导复合股线的准静态应力-应变曲线和能量耗散具有很强的非线性. 同时, 考虑塑性应变产生的损伤退化, 推导了卸载过程中非线性和线性卸载模量, 提出了考虑损伤的双曲面弹塑性本构模型来预测准静态加卸载应力-应变响应和能量耗散; 通过疲劳损伤演化模型分析和预测Nb_3Sn超导复合股线在77 K和300 K下疲劳过程中的能量耗散. 理论与实验结果对比表明: 准静态加卸载拉伸实验中损伤退化是能量损耗产生非线性的主要原因. 此外, 对Nb_3Sn超导复合股线的疲劳断裂模式进行了分析, 结果表明: Nb_3Sn芯丝组在77 K时表现为脆性断裂, 在300 K时表现为韧性断裂. 这些新发现为研究Nb_3Sn超导复合股线的非线性力学行为提供了新的视角.